An inverse analysis method for determining abradable constitutive properties

Ryan Lye [a], Chris Bennett [a,*], James Rouse [a], Giuseppe Zumpano [b]

[a] *Gas Turbine and Transmissions Research Centre, Faculty of Engineering, University of Nottingham, Nottingham, UK*
[b] *Rolls-Royce PLC, P.O. Box 31, Derby DE24 8BJ, UK*

ARTICLE INFO

ABSTRACT

Abradable coatings enable small tip clearances within gas turbine engines to be achieved. These coatings allow blades to cut their ideal paths during engine running-in and act as a sacrificial layer during unforeseen blade-casing interactions, minimising any damage to the blades. Abradables are often plasma sprayed and as a result, a given abradable can have a wide range of properties which are defined by its composition and the spray process parameters. These properties are also known to evolve during blade-casing interactions as a result of heating and compaction. In industry, abradables are often characterised by a superficial Rockwell hardness value; however, it is not clear how the Rockwell hardness relates to the mechanical properties of the abradable or whether this relationship is unique. An inverse methodology is presented for obtaining these properties via simulated Rockwell hardness testing. Firstly, a neural network (NN) is trained using the simulated Rockwell tests, which is then used in conjunction with a particle swarm optimisation (PSO) to estimate abradable properties for a given hardness value. These properties, determined from the optimisation process, are then used to conduct a series of blade-casing interaction simulations, demonstrating how the contact forces and dominant frequencies differ during rub events. This work provides a methodology to rapidly estimate abradable properties over their full range of acceptable hardnesses, which can in turn be used to optimise specific blade geometries and abradable hardnesses to produce optimal compressor performance and blade life.

1. Introduction

In order to improve aeroengine efficiency, the clearances between blade tips and the surrounding casing are minimised to create an increase the overall pressure ratio (OPR), gas temperatures, and gas pressure, which in turn increase thermal efficiency [1,2]. Inevitably, the reduced blade tip clearance leads to more frequent blade-casing interactions, referred to as rub events from here on, and therefore it is now common practice to plasma spray the internal surface of the casing with an abradable material. These abradable coatings are intended to reduce the severity of rub events and to wear preferentially to the blade. For the Low Pressure Compressor (LPC) and Intermediate Pressure Compressor (IPC), at temperatures of up to 345 °C, an Aluminium Silicon Polyester (AlSi-PES) abradable is commonly used in conjunction with Ti-6Al-4V blades ; however, there is a degree of uncertainty surrounding abradable material properties and how they influence the outcomes of, and develop during rub events.

In order to understand the influence of abradable composition on the wear and damage mechanisms during blade-casing interactions, a wide range of experimental studies have been carried out. However, typically only the hardness is used to characterise a newly sprayed abradable, leaving open questions about the constitutive behaviour of individual phases and the bulk homogenised properties, and the link between these properties and the behaviour during rub events. Regarding the constitutive properties of AlSi-PES abradables, several investigations have been conducted over a range of strain rates and temperatures through quasi-static compression and Split-Hopkinson Pressure Bar (SHPB) testing [4–6]. Chevrier et al. [7] then used these results along with complimentary work to fit both a standard and modified Johnson-Cook damage model capable of predicting failure of specimens over a range of temperatures in both quasi-static and dynamic regimes. While these tests give valuable information for modelling, they do not capture the variability in abradable properties introduced at the system level or between spray batches. Regarding testing of blade-casing interactions, a large emphasis has been placed on the characterisation of the interaction itself. Fois et al. [8] investigated the effects of the hardness of an AlSi
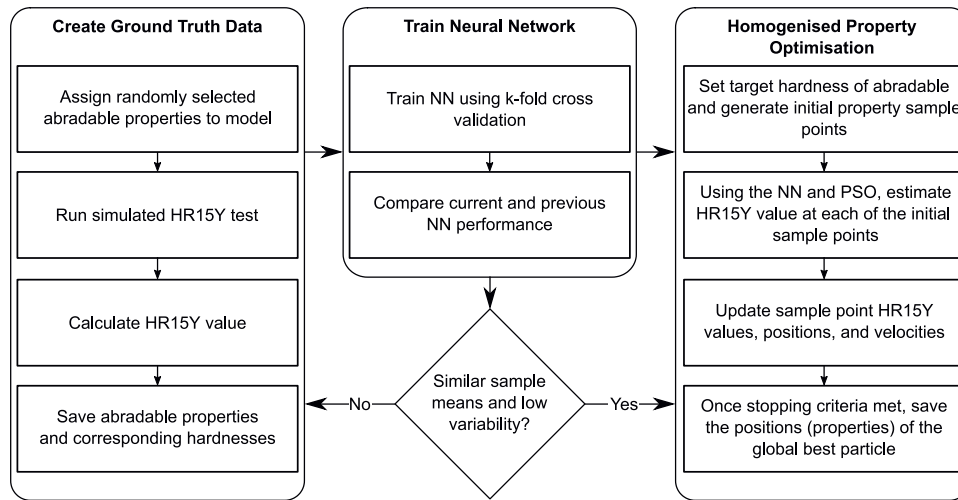
Fig. 1. Workflow of property optimisation process.

hexagonal boron nitride (AlSi-hBN) on rub events with a Ti-6Al-4V blade. It was concluded that abradable hardness dictates the wear and damage mechanisms at low incursion rates. Watson and Marshall [9] studied the wear mechanisms for different abradable batches and hardnesses and concluded that harder abradables lead to lower abradability and more blade abrasive wear. Yi et al. [10] suggested that increased abradable hardness leads to a decrease in abradability, and that abradables of similar hardnesses but with different compositions produce significantly different results. Therefore, it was said that abradability cannot be judged by a single hardness alone.

It is known that like abradables of various hardnesses interact differently with blades during contact, and studies have given phenomenological explanations for this. From an experimental standpoint there is limited work on the determination of the mechanical properties of an abradable, or on how damage accumulates over the full range of acceptable hardnesses. Understanding the constitutive behaviour of the abradable is important in being able to link the manufacture and design of the system to the behaviour of rub events, which will then allow the system to be optimised. Hardness alone is not a useful bulk measurement when modelling the behaviour of a system but is a very cheap test to conduct. This work aims to provide a method capable of predicting homogenised abradable properties over a range of hardnesses to begin to bridge this gap.

From a modelling perspective, there has been an effort to determine the homogenised material properties from abradable micrographs, to couple what happens on the macroscale with the microscale. Faraoun et al. [11] used object oriented finite element analysis (OOF) to obtain a 2D geometry suitable for analysis from an AlSi-hBN micrograph image. It was also shown via a bending test how the Young's Modulus of AlSi decreases by up to 76 % when plasma sprayed in comparison to the same material when cast. The obtained material values were then assigned to the 2D geometry, and a tensile test conducted to find the homogenised Young's Modulus and Poisson's ratio. Similarly, Duramou et al. [12] used a finite element (FE) model to determine a relationship between the microstructure of atmospheric plasma sprayed AlSi-PES and its mechanical properties. Nano-Hardness Tests (NHT) were conducted to determine the Young's Modulus for both the AlSi and PES phases. These properties were then applied to several 2D geometries created from different micrographs, simulated uniaxial tensile tests conducted, and then the average Young's Modulus and Poisson's ratio were taken to be the homogenised elastic properties. Bolot et al. [13] created 2D geometries for simulation directly from AlSi-PES micrographs without simplification using a one cell per pixel approach, where each cell corresponds to either the AlSi matrix or PES filler phases. This enabled the effects of particle orientation to be considered in thermal and

mechanical testing. It was found that particle orientation had a significant effect on thermal characteristics but not so for the Young's Modulus. Cheng et al. [14] used a 3D finite element model created through x-ray computed tomography to capture the complex behaviour of an AlSi-PES abradable such as damage in the AlSi and PES phases in addition to debonding of the phases. The model was calibrated against experimental tensile and compressive tests and the output stress strain curves from the experiments and models were in good agreement. However, these methods derive their FE geometries directly from micrographs and with the exception of Cheng et al. [14] only account for elastic properties, which limits their use in compressor blade tip rub simulations. By directly using micrographs, abradables of each hardness are needed to analyse and determine the elastic properties. Furthermore, the constituent properties will vary depending on the hardness of the abradable meaning that fixed properties cannot be used.

Neural Networks (NNs) have gained a lot of interest in many fields for their flexibility, speed, and relative ease of implementation. A NN provides a means to find patterns in data through a learning processes that adjusts weights and biases so that the error between its outputs and ground truth training data is minimised. There are several types of NN such as the fully connected feedforward multilayer perceptrons (MLPs), convolutional neural networks (CNNs) often used for image analysis and classification, recurrent neural networks (RNNs) which use temporal or sequential data, and more recently generative adversarial networks (GANs) which are able to create new data that resembles that of the training set. The flexibility of NNs in a materials science context have been demonstrated in recent works with applications ranging from modelling the influence of chemical compositions, hardnesses and temperatures on a materials response [15,16], predicting chemical compositions of steel from its mechanical properties [17], and to predicting the local stress fields in materials with microstructural features [18].

This study presents a methodology to determine the material properties of plasma sprayed abradables over their full range of acceptable hardnesses via an inverse optimisation process. These optimised properties are then used to simulate blade-casing interactions between a Ti-6Al-4V blade and an AlSi-PES abradable. In doing this, the gap between bulk hardness measurements and useful constituent properties is closed. Finally, the ability to simulate blade-casing interactions over a wide range of abradable hardnesses will allow specific blade geometries to be paired with an optimum abradable specification.

2. Methodology

Abradables are typically plasma sprayed onto the target substrate,
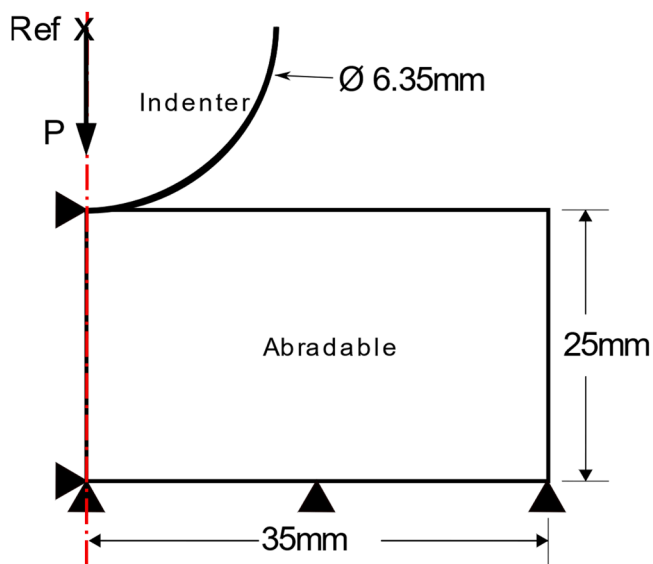
Fig. 2. Schematic of the axisymmetric HR15Y indentation model.

Table 1
Homogenised material property bounds.

AlSi-PES property bounds		
	Lower Bound	Upper Bound
$E[MPa]$	2000 [23]	18,000 [11]
$\sigma_y[MPa]$	5 [4,23,24]	50
$K[MPa]$	100	1000
ν	0.05	0.2
n	0.3	0.7

which can lead to wide variations of abradable properties between batches [9,19]. A superficial Rockwell hardness test (HR15Y) is often used to quickly determine if a given abradable is within some generally broad required bounds. However, abradable properties can vary greatly over the full spectrum of allowable hardnesses [9,20] which in turn leads to non-optimal blade and abradable pairings, that is, an abradable which minimises contact forces and the excitation of undesirable modes has not been chosen for a specific blade geometry. A method for estimating the homogenised abradable properties from a single HR15Y value has been developed to allow specific blade geometries and abradable hardnesses to be effectively tuned. This enables the allowable HR15Y ranges for specific blade geometries to be refined and optimal performance achieved.

The workflow for this method is summarised in Fig. 1, where the key stages of the homogenised property optimisation are outlined. Firstly, a set of ground truth data was gathered using an axisymmetric model in Abaqus to simulate HR15Y tests. To do this, batches of abradable properties were generated within predefined bounds using Latin Hypercube Sampling (LHS), ensuring near random selections with good variability. These generated properties were then used in the simulated HR15Y tests from which the hardness was calculated and saved along with the corresponding abradable properties.

Secondly, the batches of ground truth data were used to train a neural network which has significant speed advantages over Finite Element Analysis (FEA). As the training data sample size is small a k-fold cross validation method was used which ensures the model is well generalised. The process of gathering ground truth data and training the NN continued until there was no significant difference between the last and current training dataset size. This ensures no more ground truth data than necessary is gathered and that the NN generalises the parameter space rather than learning the training data.

Finally, a set of homogenised material properties were determined using Particle Swarm Optimisation (PSO) in conjunction with the NN. PSO has been chosen for its ability to effectively find the best global solution. This optimisation process minimises the difference between a user defined target hardness and predicted hardness for a given set of input parameters. Once each of the particles converged on a single solution, the optimisation ended and the predicted homogenised properties were saved.

Upon completion of the property optimisation, a series of blade-casing interaction simulations were run to test the significance of abradable properties on these interactions. For the blade, a NACA 9406 geometry was used. From these models, the differences in contact forces and dominant blade modes due to different abradable hardnesses were identified.

2.1. Ground truth data collection

To generate the ground truth data an axisymmetric FEA model of a HR15Y test was created and is schematically shown in Fig. 2. Eight node reduced integration axisymmetric elements were used for the abradable and in the contact region had a size of 0.1×0.1 mm while the indenter was an analytical rigid body. The indenter was constrained so that it could only move vertically, while the left edge and bottom edge of the abradable were constrained so that there was no horizontal or vertical movement respectively. The model comprised a rigid 6.35 mm (half inch) ball indenter and 70 mm diameter abradable section with a height of 25 mm, the large abradable size was chosen to ensure boundary conditions did not heavily influence the results. The load was applied to the reference point on the indenter in 3 stages, initial pre-load (29 N), max test load (147 N), and final test load (29 N) in accordance with ISO 6508-1 [21.22]. A friction coefficient between the indenter and abradable of 0.47 was chosen [3].

LHS has been used to generate near random homogenised abradable properties in batches of 150 with good variability. The lower and upper bounds of the variables used are shown in Table 1. These property bounds reflect the properties of the abradable constituent phases, with the lower and upper bounds representing an abradable made only of PES or plasma sprayed AlSi respectively, doing this keeps the area of interest as large as possible. This method could be extended to other abradables that are often subjected to Rockwell hardness testing by changing these boundaries to reflect the new constituent phases, or if the phase volume fractions are known the Voigt Reuss bounds could also be used. Often, abradable properties are given without mentioning the hardness of the abradable to which they belong or were derived from, so it is important to describe how the homogenised properties vary with hardness. For each sample in a batch, an HR15Y test was simulated, and the hardness calculated as shown in Eq. (1), where h is the difference in indentation depth between the max test load and final test load. Following this, the hardness along with the corresponding abradable properties were saved.

$$Superficial \quad Rockwell \quad Hardness = 100 - \frac{h}{0.001} \qquad (1)$$

2.2. Neural network training

To train the NN, the training dataset size was increased incrementally by 150 sample points until the current and previous iterations' sample means and variability were statistically the same as determined with a t-test and f-test. This has two main benefits, firstly the training set size is kept as small as possible while not losing NN accuracy. Secondly, the training set is not too large ensuring that the NN is well generalised and not learning the training set (overfitting). A k-fold cross validation method was used to train the NN with 10 data set splits, which is particularly important for small data sets as it allows all observations to appear in the training set and provides a truer representation of the network's accuracy.
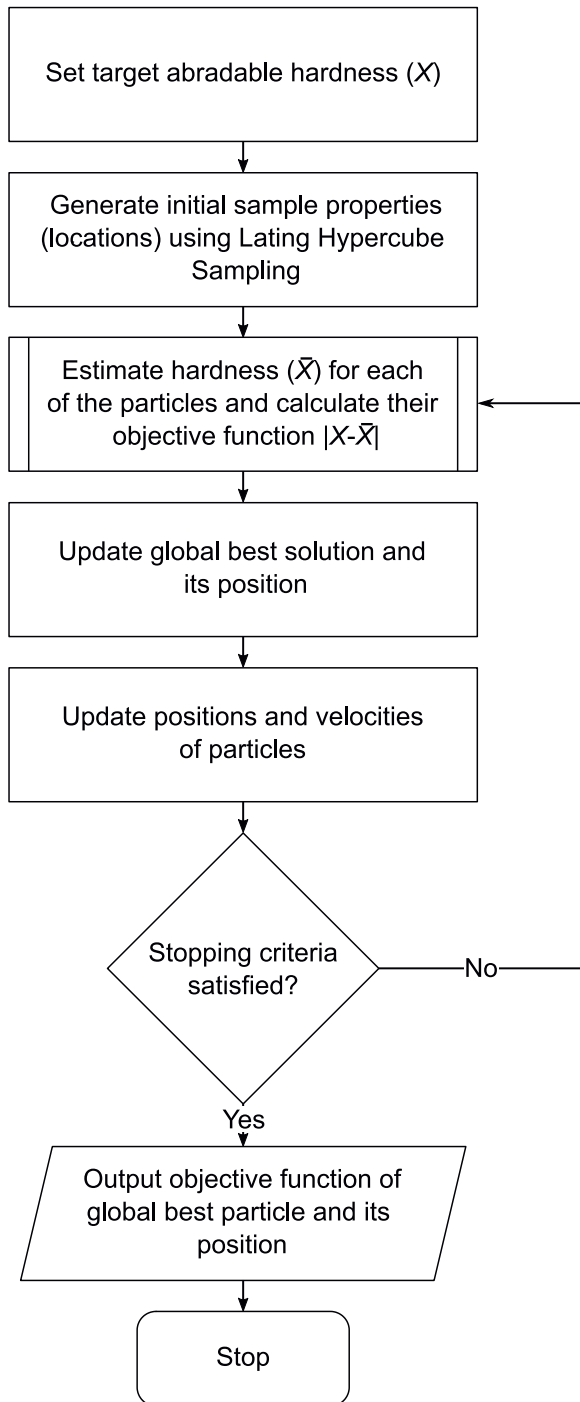
Fig. 3. Flowchart of the homogenised property optimisation process.

The training was limited to 2000 epochs with a batch size of 32 and patience of 150. The validation loss Mean Squared Error (MSE) was minimised, and the minimum change monitored was 1×10^{-6}, that is, if no change greater than this is seen in the next 150 epochs the training stops and the NN is saved. The model architecture simply comprised 5 input nodes, 1 hidden layer with 6 nodes each using a Rectified Linear Unit (ReLU) activation function, and 1 output layer with 1 node using a sigmoid activation function.

2.3. Homogenised property optimisation

The procedure used to determine the homogenised properties of an
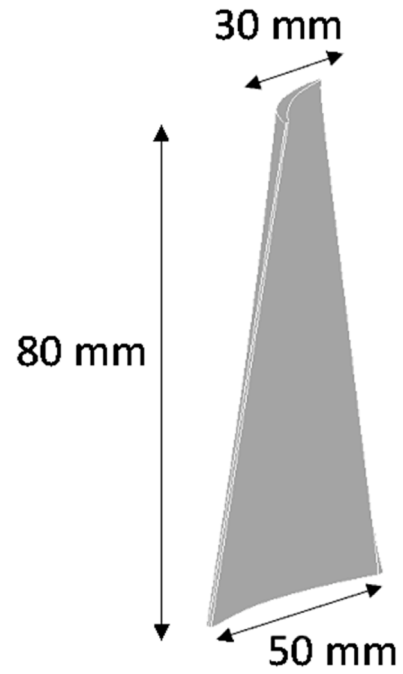
Fig. 4. Generic NACA 9406 blade.

abradable with a given Rockwell Hardness is presented in Fig. 3. To begin a target Rockwell Hardness was set, and a swarm of particles initialised using Latin Hypercube Sampling (LHS). The initial particle values of Young's Modulus, E, Poisson's ratio, ν, strength coefficient, K, strain hardening exponent, η, and yield stress, σ_y, were placed inside the property bounds previously shown. To capture post yield behaviour a power law hardening rule has been used. The homogenised material property bounds used for the NN were the same as those used to gather the training data.

Following the initial particle placement, the Rockwell Hardness for each particle was determined. From this the current objective function, defined as the absolute difference between the target hardness, X, and estimated hardness, $\overline{X}$, as shown in Eq. (2) was calculated for all particles.

$$Objective \quad Function = \quad |X - \overline{X}| \tag{2}$$

Each individual particles' best position and the global best position were saved, and then used to update the position and velocity of each particle, as shown in Eq. (3) and Eq. (4) respectively.

$$x_{t+1}^i = x_t^i + V_t^i \tag{3}$$

$$V_{t+1}^i = \omega V_t^i + r_{1t} C_1 \left(P_t^i - x_t^i \right) + r_{2t} C_2 \left(G_t^i - x_t^i \right) \tag{4}$$

Here i corresponds to the ith particle, and t is the tth iteration of the optimisation. The position of a particle i at increment t is x_t^i and similarly its velocity is V_t^i. As shown in Eq. (3), the position of particle i in the next increment is simply the sum of its current position and velocity. To calculate the updated velocity V_{t+1}^i three distinct terms were summed together which control the inertial, cognitive, and social behaviour of each particle, as shown in Eq. (4). The inertial term comprises an inertial weight ω and is multiplied by the ith particles current velocity, thus influencing the effect V_t^i has on V_{t+1}^i. Next is the cognitive term, where C_1 is the cognitive weighting, P_t^i is the best position found by the ith particle up to the current iteration, and r_{1t} is a uniformly distributed random number in $[0, 1]$. The purpose of r_{1t} is to prevent particles moving directly towards personal and global best solutions, which subsequently diversifies the particles and creates more effective searches [25]. Lastly
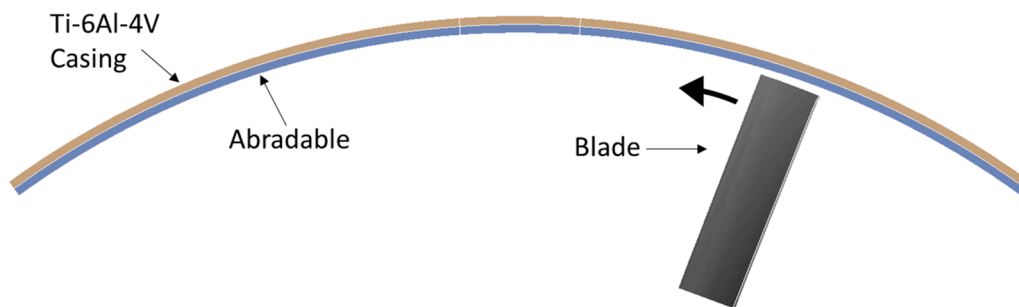
Fig. 5. Schematic representation of the blade rub model.
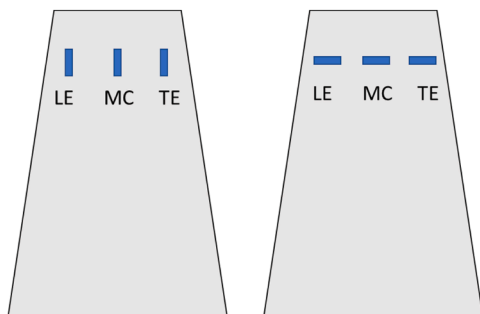
Fig. 6. Schematic representation of strain measurement positions. Left: Flap-wise; Right: Torsional.

is the social term, where C_2 is the social weighting, G_t^i the global best position found up to the current iteration by any particle, and r_{2t} is a different uniformly distributed random number in $[0,1]$. Following limited testing, ω, C_1, and C_2 were set as 0.5, 1, and 0.75 respectively. This created a cognitive swarm where each particle was influenced more so by its own history rather than that of the swarm. In general, a cognitive swarm will take longer to converge on a solution, but the parameter fields will have been better explored, increasing the

likelihood of obtaining a globally optimised solution. This process was then repeated until either the maximum number of iterations was met, or until the global best solution did not improve by more than 1×10^{-6} over the next 250 iterations.

2.4. Blade rub simulations

To examine the severity of blade-casing interactions over the range of possible abradable hardnesses a series of blade-casing rub models were run. For the Ti-6Al-4V blade, a NACA 9406 geometry was chosen, the basic dimensions of which are shown in Fig. 4, the blade tip is twisted by 25° with respect to the blade base about the mid-chord position.

The abradable section comprised an abradable liner with a Ti-6Al-4V backing, the internal radius of the abradable ring was 295 *mm* while the blade tip radius was 260 *mm* as shown in Fig. 5. This ensured a gradual contact, with the maximum incursion depth being set at 5 *μm*. An AlSi-PES abradable typically has an acceptable HR15Y value between 50 and 80 [3,9], therefore blade-casing rubs were modelled with abradable properties corresponding to each of these extremes and a mid-value of 65. AlSi-PES is found in the early compressor stages where blade tip speeds are in the order of $400 m.s^{-1}$, which is the speed that was used and equates to approximately 14,700 *rpm* [9].
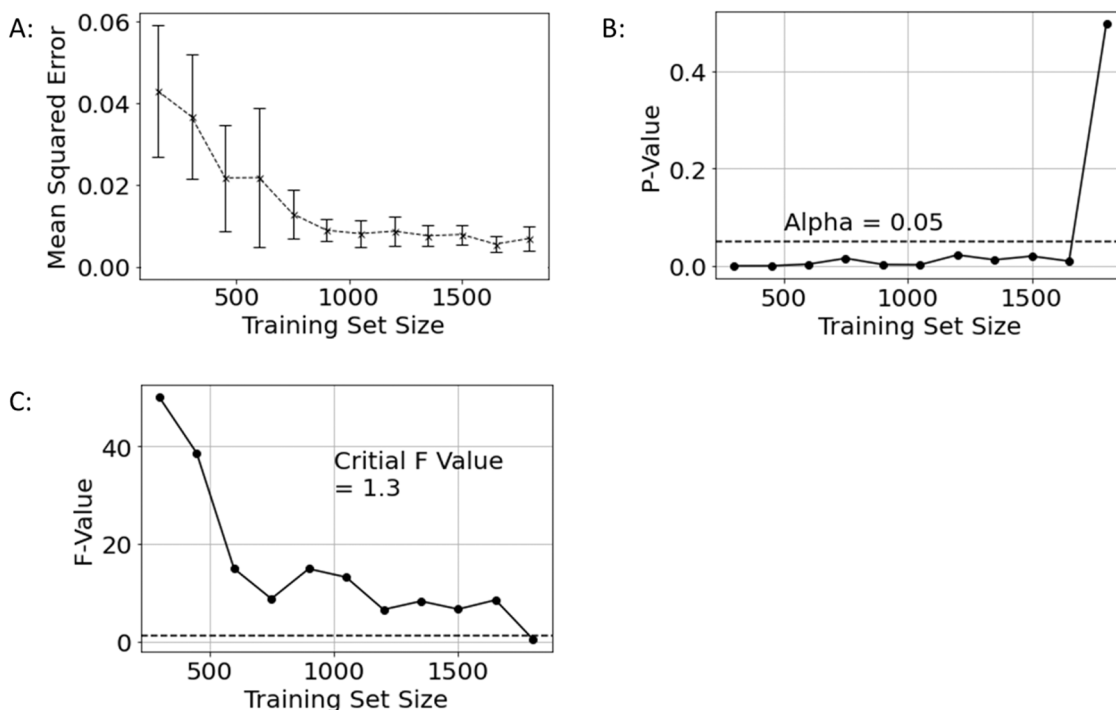
Fig. 7. A) Validation set MSEs for increasing training set sizes; B) P-values of MSEs with training set size; C) F-values of MSEs with training set size.
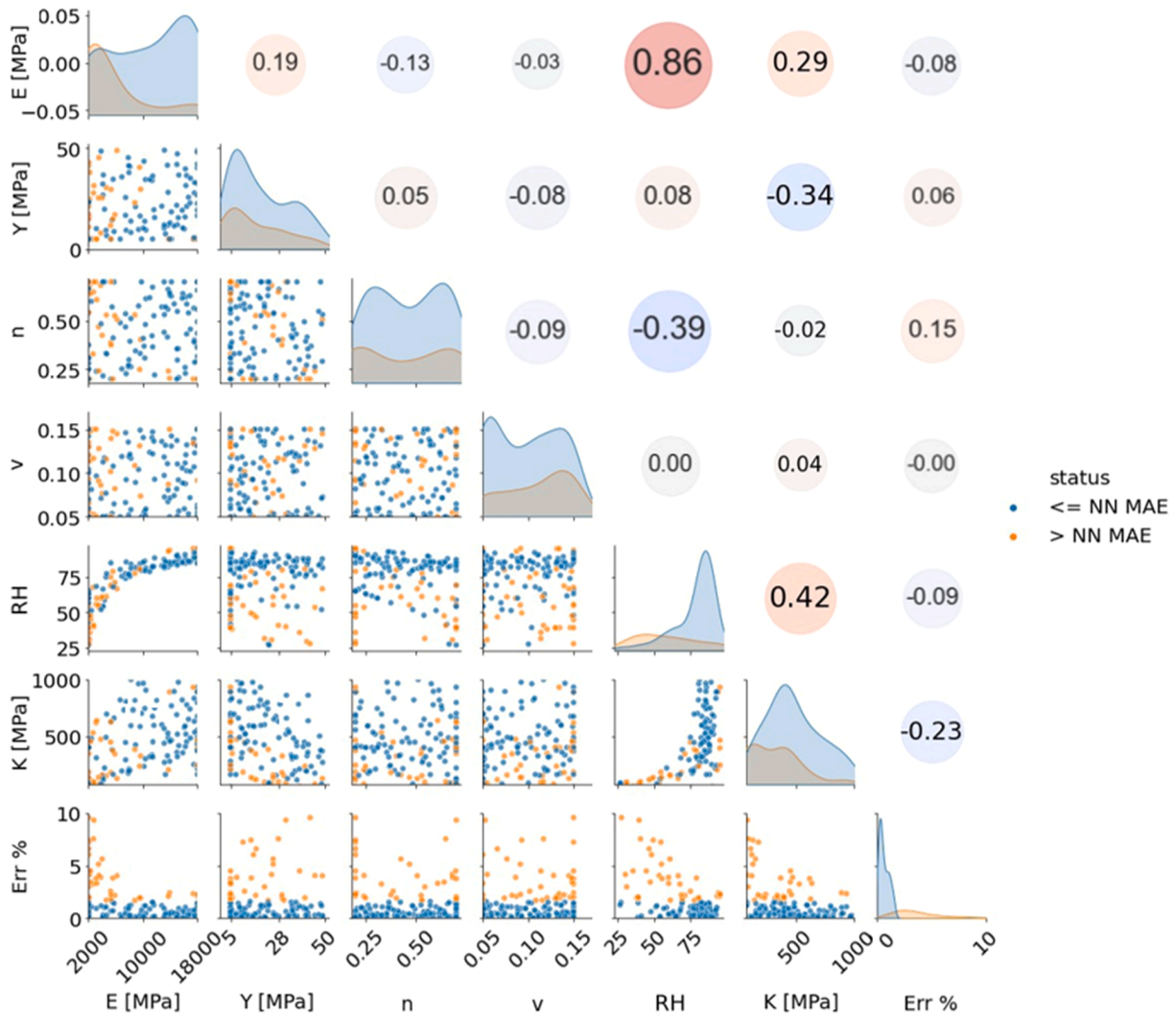
Fig. 8. Lower corner: Pairs plot with NN inputs and output absolute errors; Diagonal: Kernel density estimations; Upper corner: Pearson correlations between pairs.
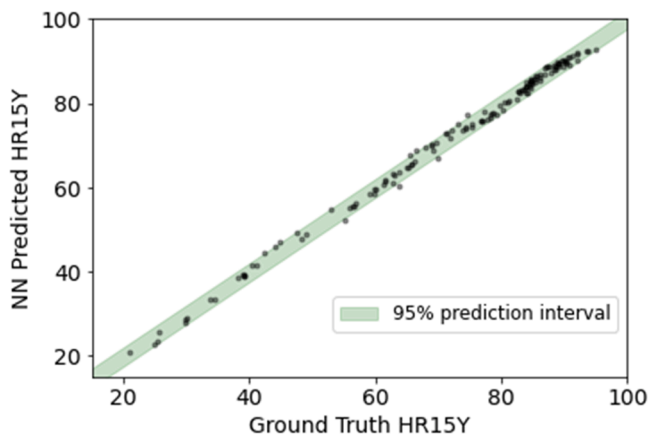
Fig. 9. Ground truth predictions vs. NN predictions.

The blade was considered as elastic with a stiffness of 110 *GPa* and Poisson's ratio of 0.3 [26]. The abradable was considered to follow Ludwik's power law hardening rule as described by Eq. (5), where σ is the post yield stress at a given strain, K is the strength coefficient, σ_y yield stress, $\varepsilon_{plastic}$ is strain after yield, and n the strain hardening exponent.

$$\sigma = \sigma_y + K\left(\varepsilon_{plastic}\right)^n \tag{5}$$

Upon completion of the blade rub models, strains aligned with (flapwise) and perpendicular (torsional) to the blade height at the leading edge (LE), mid-chord (MC), and trailing edge (TE) were obtained, shown in Fig. 6. This strain data was then processed using a Wavelet Synchrosqueezed Transform (WSST), which has the benefit of having good time resolution at high frequencies enabling the detection of highly transient signal components. These WSSTs were then plotted and compared to each other and to the blade's natural frequencies at the test speed, showing how the dominant frequencies evolve over time for each of the hardnesses at the three previously mentioned locations. The resultant contact forces at the blade tip were also extracted from the model, and the peak loads found.

3. Results and discussion

A NN was trained using ground truth data gathered from simulated HR15Y tests with the number of training points being determined by a convergence study. The NN was then used to estimate homogenised AlSi-PES abradable properties through the range of its acceptable hardness values. These estimated homogenised properties are compared to those in the literature and used to model blade-casing interactions.
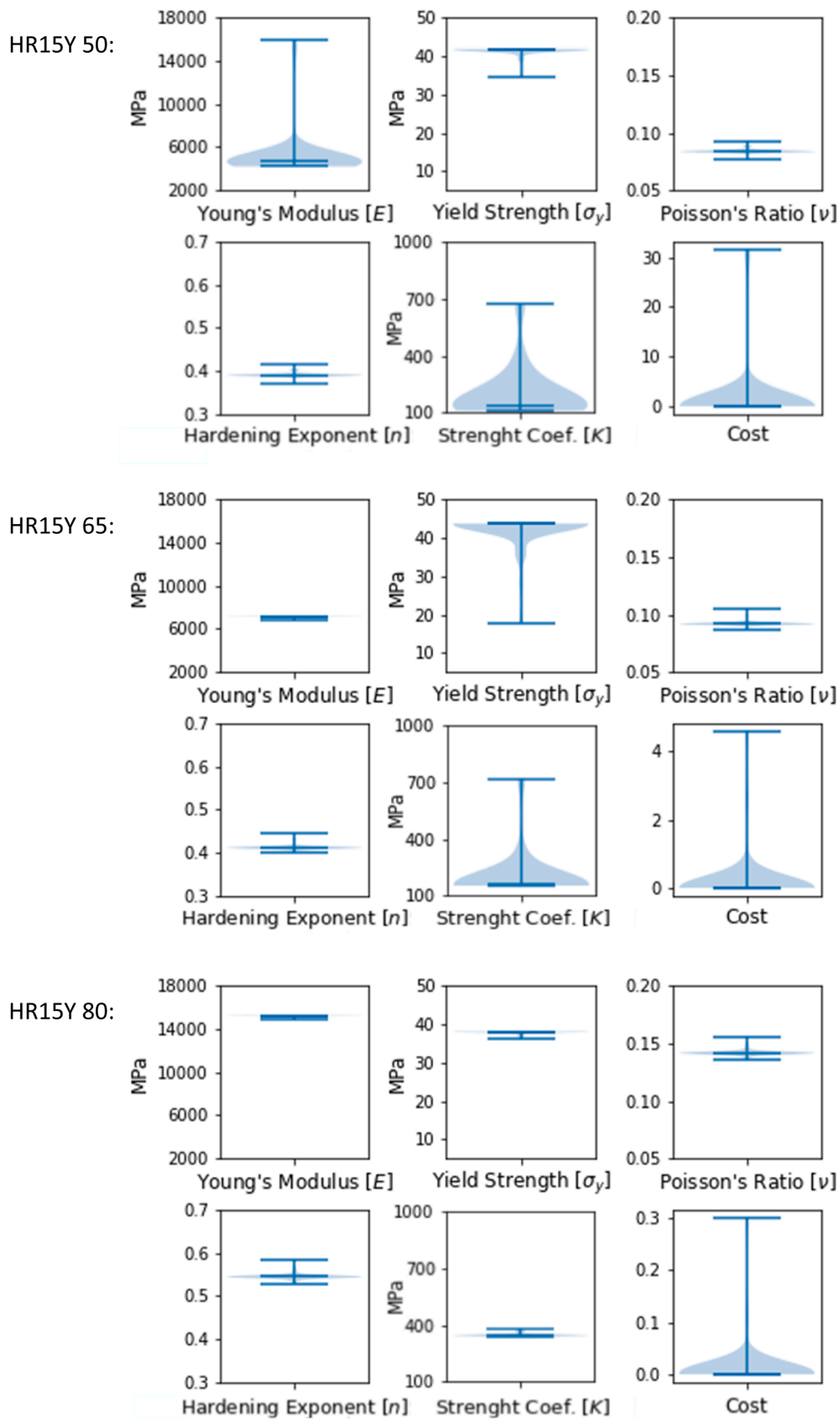
Fig. 10. Violin plots showing the particle distributions for each of the optimisation inputs in addition to the cost distribution. Top HR15Y 50; Middle HR15Y 65; Bottom HR15Y 80.

Table 2
Homogenised material properties from Rockwell Hardness NN.

Rockwell Hardness	$E_{homogenised}$ [MPa]	$\sigma_{y,homogenised}$ [MPa]	$K_{homogenised}$ [MPa]	$n_{homogenised}$	$\nu_{homogenised}$
50	4687	42	115	0.39	0.087
65	7163	44	149	0.41	0.095
80	15240	38	390	0.54	0.14
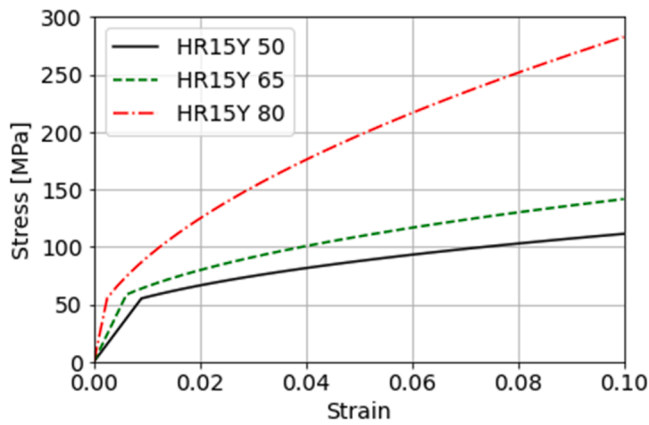
Fig. 11. Corresponding stress-strain curves for each hardness.

Table 3
Natural frequencies for the generic NACA 9406 blade.

Mode	1st Flap	1st Torsion	2nd Flap	2nd Torsion	Edgewise	3rd Torsion
Frequency [Hz]	811	2069	3125	4358	5855	6561

3.1. Neural network behaviour

From the NN training convergence study, the NN validation losses begin to plateau at 900 training points as shown in Fig. 7a. The results of the t-test and f-test, used to determine if any statistically significant differences existed between the maximum and second largest datasets sample means and variability respectively, are shown in Fig. 7b and c. For the t-test, the alpha value was set at 5 % and the first point with a p-value greater than this had a training set size of 1800. Similarly, the f-value was also less than the critical value with this training set size. Therefore, a training set size of 1800 was used as statistically significant improvements with respect to the previous set size were not seen.

A set of 140 blind data points were also fed through the newly trained network so the absolute error in hardness predictions for previously unseen data could be calculated. Each of the inputs and the absolute error of each prediction could then be plotted in a pairs plot, shown in Fig. 8. The absolute errors were then compared to the validation Mean Absolute Error (MEA) of the NN which was 1.7 %, the predictions with errors smaller than or equal to the network are shown in blue and those errors larger than the network are shown in orange. It can clearly be seen that the network is well generalised and that the network has can perform well over the entire range of possible input properties, and that the vast majority of errors were less than 5 %. Additionally, the largest of these errors occur at the lowest stiffnesses and measured hardnesses, this is not seen as an issue as these low hardnesses are outside of acceptable limits. The accuracy of the hardness predictions alone is perhaps easier to see in Fig. 9, here the NN predictions are plotted against the FEA ground truth hardness. The strong agreement is clear, with almost all of the points falling within the 95 % confidence interval over the full range of hardnesses.

The upper right-hand corner of Fig. 8 shows the Pearson correlations of the pairs with better than or equal to NN MAE. Here the stiffness is seen to be the most dominant input variable and has a strong positive correlation with the measured hardness. This can also be seen in the similar correlations for the stiffness and hardness versus the error. Furthermore, the Poisson's ratio appears to have no correlation with increasing hardness, indicating that in future studies this value can be fixed and omitted from the optimisation.

Additionally, the network was significantly quicker. Using FEA, the time to compute the hardnesses of 50 different abradables was in the order of 1 hour, whereas the network took approximately 1.5 seconds, a speed increase of 2400 times. This significant speed advantage enabled much larger particle swarms to be ran for longer, increasing the likelihood of all the particles finding and converging on the global best solution.

3.2. Particle swarm optimisation

Using the NN to estimate the Rockwell Hardness at each of the particle coordinates during the PSO proved effective. As shown by the violin plots in Fig 10, each of the particles generally converged for all of the properties for each hardness, this implies that a global best solution has been found. Some apparent exceptions to this are the Young's Modulus and strength coefficient for HR15Y 50 and the yield stress and strength coefficient for HR15Y 65, with a large disparity between the minimum and maximum values. However, it can be seen that the majority of particles are distributed around the mean indicating that they are in close proximity to the global best solution. Interestingly the PSO appeared to quickly find the global best solution, but the cognitive nature of the swarm meant that run times were in the order of 500 – 1000 iterations, rather than a few tens of iterations when the global best seemed to be found.

The global best solutions for each of the hardnesses investigated are presented in Table 2. These stiffnesses are consistent with those reported in the literature. Duramou et al. [12] reported E to be 7.9 *GPa* via FE simulations and confirmed this by means of a bending test which gave a value of 7 *GPa*. Using a one cell per pixel approach to directly recreate an AlSi-PES abradables microstructure from its micrograph for FE simulations without geometric simplification, Bolot et al. [13] reported E_x and E_y to be 7.6 *GPa* and 6.1 *GPa* respectively. The stress-strain curves for each of the considered hardness are shown in Fig. 11. For the HR15Y 50 and 65 curves there is little difference in the strain hardening rate and yield stress, with the most pronounced change being in the stiffness, as expected given that this is the most dominant input variable. For HR15Y 80 there again is a significant change in the stiffness in addition to the strain hardening exponent, and not significant change in the yield strength. In fact, one might have expected the yield strength to increase as the physical material would contain less of the dislocator phase and porosities. This is likely an artefact of there being no damage in the indentation model, and with the high stiffness a lower yield stress was needed to ensure yielding did occur and that a HR15Y value of 100 was not returned.

3.3. Blade-casing interactions

To begin the natural frequencies of the blade at the test speed of 14,700 *rpm* were found and are shown in Table 3, 3rd torsion is the highest mode considered as subsequent modes approach the output frequency of the model data meaning that the Nyquist rule cannot be followed when sampling the data.

The raw flapwise and torsional strain data for each of the hardnesses and positions was processed using WSSTs as shown in the Appendix, while the flapwise LE and torsional MC WSSTs that showed the greatest variation across the hardnesses are shown in Fig. 12. It can be seen that the excited frequencies seen in the flapwise direction are similar, with the biggest difference being in the high energy modes. That is, for
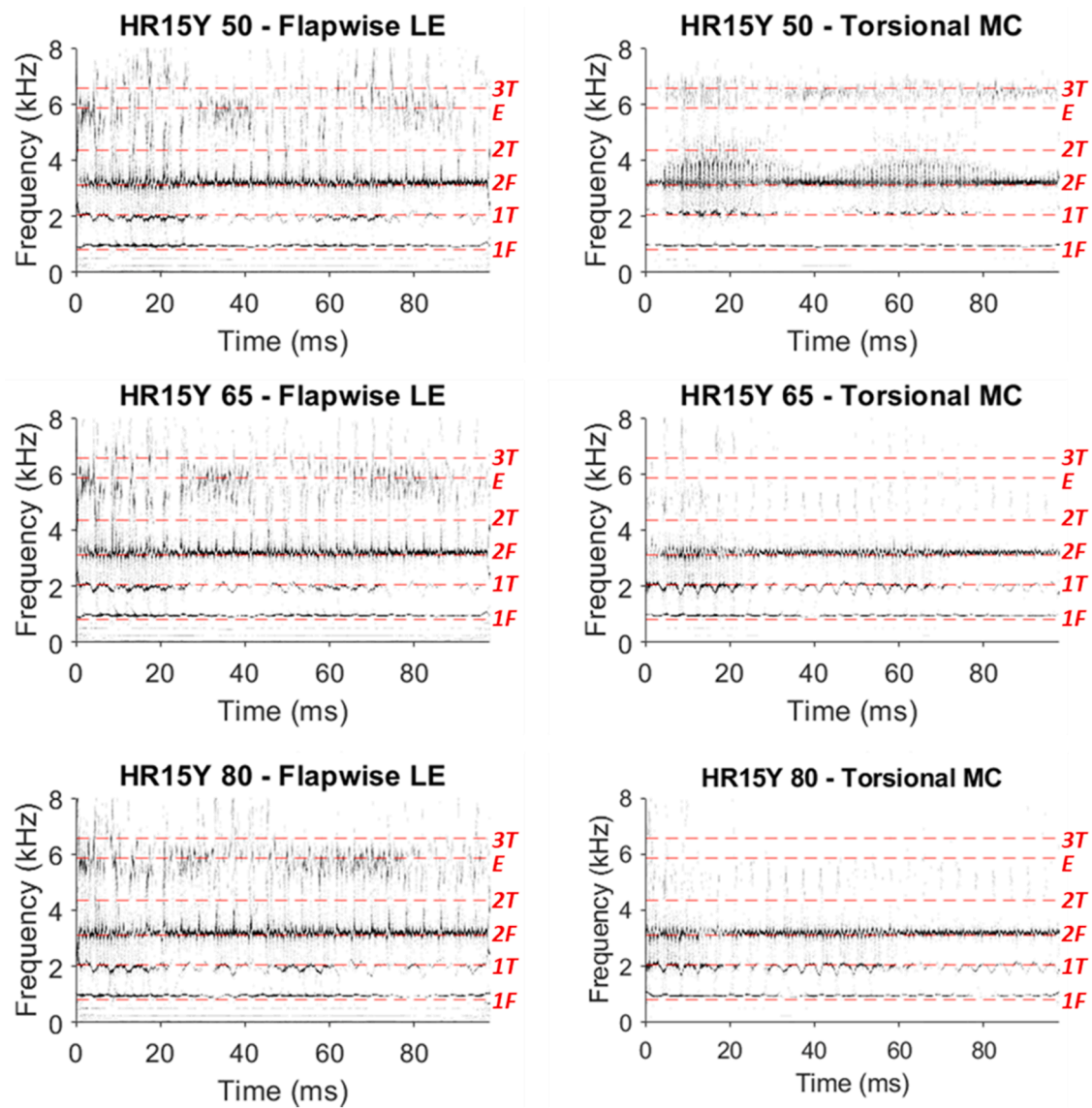
Fig. 12. WSST plots for all hardnesses. Left: Flapwise LE; Right: Torsional MC.
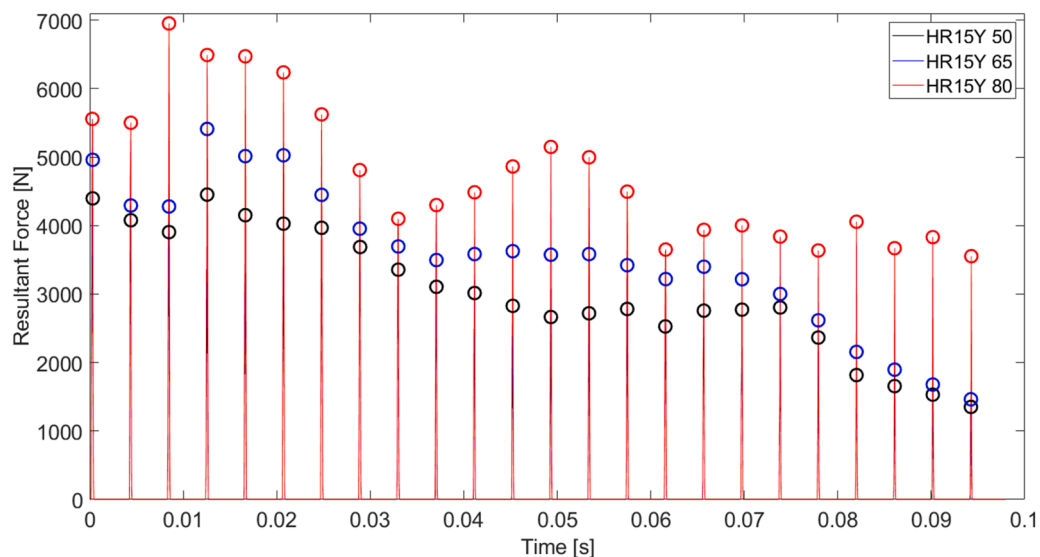
Fig. 13. Contact forces for all tested abradables with the peak contact forces highlighted.

HR15Y 80 the frequencies corresponding to the edgewise mode are more pronounced particularly between 50 and 80 *ms than* in the softer abradables. A potential cause for this is that more energy was being put into the blade with harder abradables due to the increased contact forces, seen in Fig. 13. Additionally, for the softest abradable there appears to be a much greater variation in the dominant modes at the highest frequencies suggesting that some mode mixing was perhaps occurring between the edgewise and 3rd torsional modes. With respect to the strains measured in the torsional direction, the differences are clear across the hardnesses, namely the changes around 2nd flap and 3rd torsion. For the HR15Y 50 abradable the frequencies corresponding to the 2nd flapwise and torsional modes were poorly resolved between 10 and 80 *ms* inferring both of these modes are present. Interestingly, there is also a distinctive band at 3rd torsion which is barely visible and not at all visible for HR15Y 65 and 80 respectively. The more pronounced frequency bands around the 2nd and 3rd torsional modes for the softest abradable implies that more torsional loading was being put into the blade by contacts that were initiated either at the LE or TE, rather than equally across the blade tip chord length. This is expected for the softer abradables, as they yield easily producing an uneven contact abradable surface for the following rubs. The majority of the flapwise modes are seen at the LE as the MC is the thickest point of the blade so minimal bending in the flapwise direction is seen here, while the MC is where the blade naturally twists around so torsional strains are well defined here.

As previously mentioned, another important difference is the contact forces seen during rub events, as they provide insight to the energy put into the blade. In the case of this elastic blade, higher contact forces simply produced vibrations with greater amplitudes. The resultant contact forces during these blade-casing interaction models are shown in Fig. 13. For the two softest abradables, there was a downward trend in the resultant contact forces as the abradable yields with little strain hardening, so rubs are shallower resulting in smaller radial forces pushing the blade tip down. Conversely, the hardest abradable did not yield as easily and when it did, there was significant strain hardening, hence the reduction in contact forces as a result of shallower rubs are partially negated by the high strain hardening rate.

From this we can begin to conclude that for the NACA 9406 blade at 14,700 *rpm* the abradable with a hardness of HR15Y 65 is best as it has the same low resultant contact forces as the softest abradable but without exciting additional torsional modes. It is worth noting that this work aimed to begin bridging the gap between the bulk hardness measurements commonly used to categorise abradables and how these are linked to the constitutive properties of the abradables. A single set of properties are often used to describe an abradable and this work has shown the importance using representative properties across all hardnesses so that blade and abradable systems can be optimised. In future work particular attention needs to be paid to the particular damage mechanisms in the abradable. Also, when running blade-casing interaction simulations attention to abradable removal and evolving properties from, for example, compaction or frictional heating needs to be considered.

4. Conclusions

This present study provides a method for estimating the homogenised properties of an abradable for a given HR15Y hardness via an inverse optimisation procedure using PSO and a NN. These optimised properties were then used to simulate blade-casing interactions between a Ti-6Al-4V blade and an AlSi-PES abradable. This has provided a link between a commonly used bulk hardness measurement and useful constituent properties. The ability to simulate blade-casing interactions over a wide range of abradable hardnesses will allow specific blade geometries to be paired with an optimum abradable specification. This study has shown that a well generalised NN is capable of estimating the homogenised properties of an abradable with a given HR15Y hardness, and when combined with PSO it is able to quickly find the global best set of homogenised properties. The set of blade-casing interaction studies have shown that subtle differences in the dominant frequencies can be seen, which can be described by how softer abradables yield more easily leading to non-uniform contacts across the blade tip chord length. Furthermore, substantial differences in the resultant contact forces for different hardness abradables have been seen. Overall, an efficient optimisation process has been developed that is able to capture the constitutive behaviour of abradables with differing hardnesses.

In future work, the damage evolution within the abradable needs to be considered to capture the debonding of particles. Also, future blade-casing interaction models will need to capture abradable removal and the evolution of abradable properties due to, for example, compaction and excessive frictional heating. Experimentally, there is a need to characterise abradables of known hardness to provide further validation and to further bridge this gap between constitutive properties that are essential for modelling and the hardness tests that are often used in industry to quickly decide if an abradable is within acceptable bounds.

CRediT authorship contribution statement

Ryan Lye: Investigation, Methodology, Writing – original draft, Formal analysis, Software. **Chris Bennett:** Conceptualization, Methodology, Supervision, Project administration, Writing – review & editing. **James Rouse:** Conceptualization, Methodology, Supervision, Project administration, Writing – review & editing. **Guiseppe Zumpano:** Supervision, Writing – review & editing.

Declaration of Competing Interest

The authors declare that they have no known competing financial interests or personal relationships that could have appeared to influence the work reported in this paper.

Data availability

The data that has been used is confidential.

Acknowledgements

Appendix A
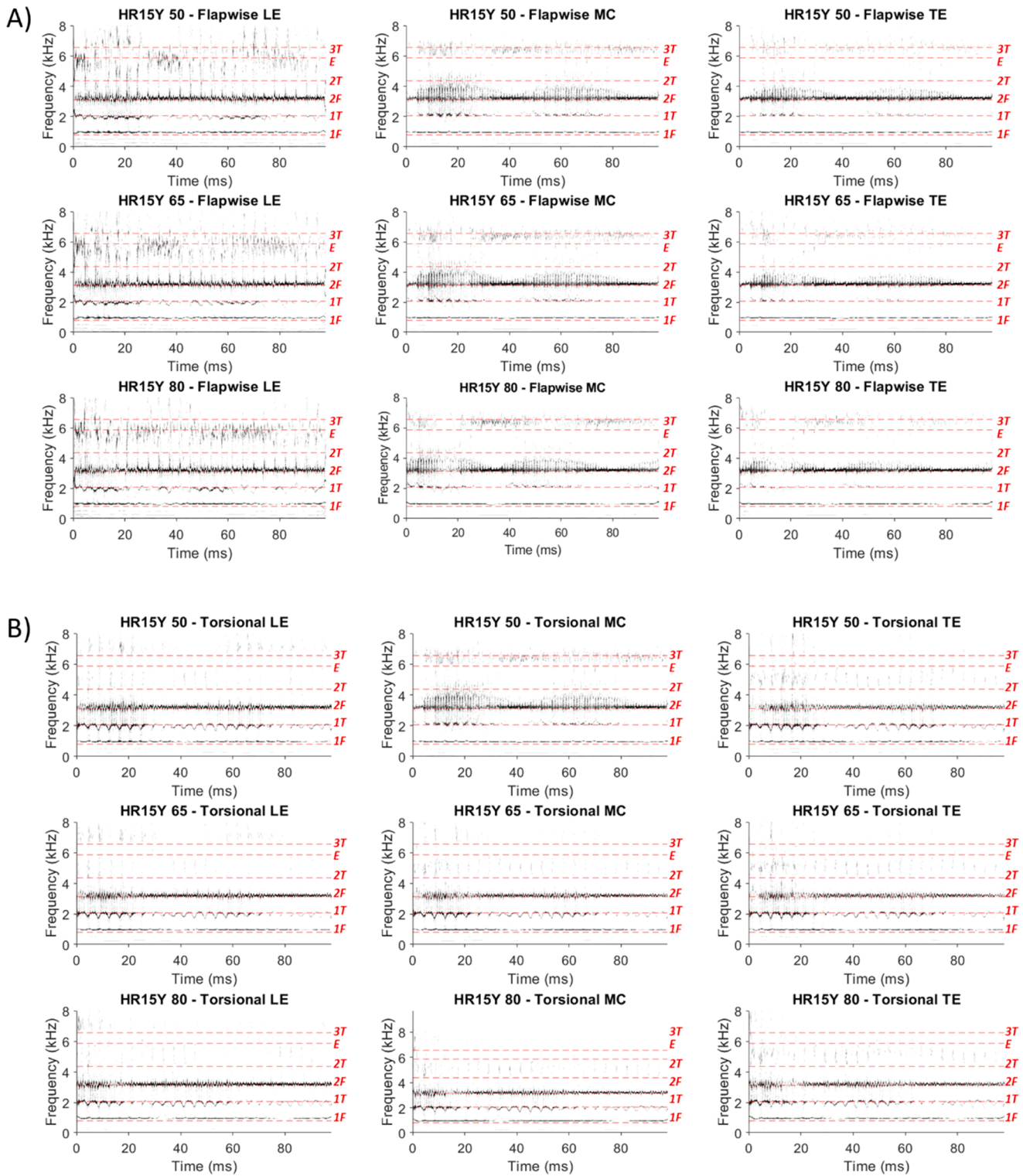
Fig. A1.

Fig. A1. WSST plots for all hardnesses and positions. A) Strains in the flapwise direction, B) Strains in the torsional direction.

References

[1] S. Nitschke, T. Wollmann, C. Ebert, T. Behnisch, A. Langkamp, T. Lang, E. Johann, M. Gude, An advanced experimental method and test rig concept for investigating the dynamic blade-tip/casing interactions under engine-like mechanical conditions, Wear 422–423 (2019) 161–166.

[2] C. Schiewe, N. Neuburger, S. Staudacher, How future propulsion systems influence future component testing: latest results from Stuttgart university's altitude test facility, in: Proceedings of the Global Power and Propulsion Society Technical Conference, 2019, 1–7. doi: 10.33737/gpps19-tc-051.

[3] Sulzer Metco, "Metco 601NS Powder Metco 601NS Aluminum-Polyester Powder." 2000.

[4] A. Pellegrino, P.M.M. Jesus, K. Dragnevski, G. Zumpano, N. Petrinic, Temperature and strain rate dependent mechanical response of METCO 601 aluminium-polyester abradable seal coating, EPJ Web Conf. 183 (2018) 1–6, https://doi.org/10.1051/epjconf/201818304012.

[5] S. Skiba, L. Faure, S. Philippon, J. Papasidero, Experimental investigation of the mechanical behavior of an AlSi-PE abradable coating at high strain rates for a large range of temperatures, J. Dyn. Behav. Mater. 6 (2) (2020) 213–223, https://doi.org/10.1007/s40870-020-00242-y.

[6] S. Skiba, B. Chevrier, L. Faure, S. Philippon, Thermoelastoviscoplastic bilinear compressive constitutive law of an AlSi-PE abradable material based on experimental investigations, J. Dyn. Behav. Mater. 7 (3) (2021) 499–508, https://doi.org/10.1007/s40870-021-00294-8.

[7] B. Chevrier, J. Vincent, L. Faure, S. Philippon, Identification of constitutive laws' parameters by means of experimental tests on AlSi-PE abradable coating, Mater. Des. 218 (2022), 110673, https://doi.org/10.1016/j.matdes.2022.110673.

[8] N. Fois, M. Watson, M.B. Marshall, The influence of material properties on the wear of abradable materials, J. Eng. Tribol. 231 (2) (2017) 240–253, https://doi.org/10.1177/1350650116649528.

[9] M. Watson, M. Marshall, Wear mechanisms at the blade tip seal interface, Wear 404–405 (2018) 176–193, https://doi.org/10.1016/j.wear.2018.03.009.

[10] M. Yi, J. He, B. Huang, H. Zhou, Friction and wear behaviour and abradability of abradable seal coating, Wear 231 (1) (1999) 47–53, https://doi.org/10.1016/S0043-1648(99)00093-9.

[11] H.I. Faraoun, J.L. Seichepine, C. Coddet, H. Aourag, J. Zwick, N. Hopkins, D. Sporer, M. Hertter, Modelling route for abradable coatings, Surf. Coat. Technol., 2006, 200 (22–23) SPEC. ISS., 6578–6582. doi: 10.1016/j.surfcoat.2005.11.105.

[12] Y. Duramou, R. Bolot, J.L. Seichepine, Y. Danlos, P. Bertrand, G. Montavon, S. Selezneff, Relationships between microstructural and mechanical properties of plasma sprayed AlSi-polyester composite coatings: application to abradable materials, Key Eng. Mater., 2014, 606 (July), 155–158. doi: 10.4028/www.scientific.net/KEM.606.155.

[13] R. Bolot, D. Aussavy, G. Montavon, Application of FEM to estimate thermo-mechanical properties of plasma sprayed composite coatings, Coatings 7 (7) (2017), https://doi.org/10.3390/coatings7070091.

[14] J. Cheng, X. Hu, D. Lancaster, X. Sun, W. Joost, Modeling deformation and failure in AlSi-polyester abradable sealcoating material using microstructure-based finite element simulation, Mater. Des. 219 (2022), https://doi.org/10.1016/j.matdes.2022.110791.

[15] A. Churyumov, A. Kazakova, T. Churyumova, Modelling of the steel high-temperature deformation behaviour using artificial neural network, Metals 12 (3) (2022), https://doi.org/10.3390/met12030447.

[16] D. Merayo, A. Rodríguez-Prieto, A.M. Camacho, Prediction of mechanical properties by artificial neural networks to characterize the plastic behavior of aluminum alloys, Materials 13 (22), 2020. doi: 10.3390/ma13225227.

[17] R. Honysz, Modeling the chemical composition of ferritic stainless steels with the use of artificial neural networks, Metals 11 (5) (2021), https://doi.org/10.3390/met11050724.

[18] V. Krokos, V. Bui Xuan, S.P.A. Bordas, P. Young, P. Kerfriden, A Bayesian multiscale CNN framework to predict local stress fields in structures with microscale features, Comput. Mech. 69 (3) (2022) 733–766, https://doi.org/10.1007/s00466-021-02112-3.

[19] P. Mallick, B. Behera, S.K. Patel, B. Swain, R. Roshan, A. Behera, Plasma spray parameters to optimize the properties of abrasion coating used in axial flow compressors of aero-engines to maintain blade tip clearance, Mater. Today Proc. (2020), https://doi.org/10.1016/j.matpr.2020.03.835.

[20] Sulzer Metco, Cause and Effect of Metco 320NS Spray Parameters for Optimization of Coating Hardness and Service Life, 2014.

[21] Metallic Materials - Rockwell Hardness Test, Part 1: Test method, ISO 6508-1:2016, 2016.

[22] S.R. Low, Rockwell Hardness Measurement of Metallic Materials, Natl. Inst. Stand. Technol., no. Special Publication 605-5, 2001, 1–116.

[23] X. Ma, A. Matthews, Evaluation of abradable seal coating mechanical properties, Wear 267 (2009) 1501–1510.

[24] Oerlikon Metco, Material Product Data Sheet CoNiCrAlY-BN / Polyester Abradable Thermal Spray Powders, 2018, 1–4.

[25] M.R. Bonyadi, Z. Michalewicz, X. Li, An analysis of the velocity updating rule of the particle swarm optimization algorithm, J. Heuristics (2014), https://doi.org/10.1007/s10732-014-9245-2.

[26] C. Leyens, M. Peters, Titanium and Titanium Alloys, Wiley-VCH, Weinheim, 2010, https://doi.org/10.1007/978-3-319-69743-7_7.